

Full paper

Superionic conductivity in lithium argyrodite solid-state electrolyte by controlled Cl-doping

Chuang Yu^{a,1}, Yong Li^{b,1}, Mathew Willans^c, Yang Zhao^a, Keegan R. Adair^a, Feipeng Zhao^a, Weihan Li^a, Sixu Deng^a, Jianwen Liang^a, Mohammad Norouzi Banis^a, Ruying Li^a, Huan Huang^d, Li Zhang^e, Rong Yang^e, Shigang Lu^e, Yining Huang^{c,**}, Xueliang Sun^{a,*}

^a Department of Mechanical and Materials Engineering, The University of Western Ontario, London, Ontario, N6A 5B9, Canada

^b Institute of Applied and Physical Chemistry and Center for Environmental Research and Sustainable Technology, University of Bremen, 28359, Bremen, Germany

^c Department of Chemistry, The University of Western Ontario, 1151 Richmond Street, London, Ontario, N6A 5B7, Canada

^d Glabat Solid-State Battery Inc., 700 Collip Circle, London, Ontario, N6G 4X8, Canada

^e China Automotive Battery Research Institute Co. Ltd, 5th Floor, No. 43, Mining Building, North Sanhuan Middle Road Haidian District, Beijing, 100088, China



ARTICLE INFO

Keywords:

Superionic conductivity
Cl-doping
Lithium argyrodite
⁷Li NMR
Solid-state batteries

ABSTRACT

The lithium ion conductivity of lithium argyrodite can be improved by introducing Cl to tailor the S/Cl disorder in the structure. An ultrafast room temperature lithium ion conductivity of up to 6.4 mS/cm was achieved for $\text{Li}_{5.7}\text{PS}_{4.7}\text{Cl}_{1.3}$. The synthesis parameters for $\text{Li}_{7-x}\text{PS}_{6-x}\text{Cl}_x$ ($x = 1.0, 1.1, 1.2, 1.3, 1.4, 1.5, 1.6, 1.7, 1.8, 1.9$) are systematically investigated to obtain pure lithium argyrodite phase with high ionic conductivity. AC impedance spectroscopy and ⁷Li spin-lattice relaxation NMR are utilized to show the enhancement of lithium ion conductivity caused by the incorporation of Cl. *Ab initio* molecular dynamics (AIMD) simulations proved that the introduction of Cl can effectively decrease the energy barriers for lithium ion migration in both short and long diffusion length scales. All-solid-state lithium batteries using LiNbO₃-coated LiNi_{0.8}Mn_{0.1}Co_{0.1}O₂ cathode and $\text{Li}_{5.7}\text{PS}_{4.7}\text{Cl}_{1.3}$ solid electrolyte display high discharge capacities and excellent cycling performances at relatively high current densities. EIS and galvanostatic intermittent titration technique (GITT) further confirm that the improved electrochemical performance can be attributed to the mitigation of voltage polarization and reduction of the interfacial resistance between the cathode and solid electrolyte.

1. Introduction

All-solid-state lithium batteries have attracted significant attention due to their potential to achieve higher energy and power densities compared to convention liquid-based Li ion batteries [1–4]. In order to achieve all-solid-state batteries with good electrochemical performance, solid electrolytes with high ionic conductivity are needed [5]. Intensive efforts have been invested to towards the exploration of high performance solid-state lithium ion conductors over the past decades [6–10]. Several families of solid electrolytes including LISICON-like [7,8], lithium garnet [11], lithium nitride [12,13], lithium perovskite [14], lithium argyrodite [15], and lithium halide [16,17] have thoroughly studied as potential candidates for use as solid electrolytes in solid-state batteries [7–9,18]. Among them, lithium argyrodite-type electrolytes

with lithium ion conductivities in the range of 10^{-2} to 10^{-3} S/cm at room temperature shows great potential due to their low cost and conductivity comparable with liquid electrolytes [15].

Lithium argyrodite has been reported to be prepared via various synthesis routes, delivering a room temperature lithium ion conductivity on the order of $\sim 10^{-3}$ S/cm [19–24]. Previous research has shown that the halogen distribution over the sulfur sub-lattice has a critical influence on the lithium ion conductivity [25]. Klerk et al. [26] have proven that the distribution of the halogen over the 4a and 4c sulfur sites determines the jump frequency of all three kinds of lithium ion jumps in the lithium argyrodite structure, i.e., doublet (48h–48h), intra-cage, and inter-cage, based on the MD simulations results. They predicted that the highest lithium ion conductivity for $\text{Li}_6\text{PS}_5\text{Cl}$ can be obtained when three-quarters of the 4c sites (and one-quarter of the 4a sites) are

* Corresponding author.

** Corresponding author.

E-mail addresses: yhuang@uwo.ca (Y. Huang), xsun9@uwo.ca (X. Sun).

¹ Joint first authors.

occupied by Cl ions. Later, this prediction was proved by tailoring the optimal amount of Br over the 4a and 4c sites close to 1/3, promoting a room temperature lithium ion conductivity of $\text{Li}_6\text{PS}_5\text{Br}$ up to 2.58×10^{-3} S/cm [21]. Furthermore, they introduced more Cl ions into the $\text{Li}_6\text{PS}_5\text{Cl}$ structure to form $\text{Li}_5\text{PS}_4\text{Cl}_2$, showing similar lithium ion conductivity values, thus revealing that increasing the halogen composition does not significantly alter lithium ion conductivity [26]. However, a number of questions related to this vacancy design strategy for lithium argyrodite remain unclear, including the relationship between the Cl amount and the synthesis routes, structure, ionic conductivity, and lithium diffusion behavior.

In this work, detailed synthesis processes for lithium argyrodite solid-state electrolytes are studied. The optimal synthesis conditions and composition to obtain the highest lithium ion conductivity for $\text{Li}_{7-x}\text{PS}_{6-x}\text{Cl}_x$ ($x = 1.1, 1.2, 1.3, 1.4, 1.5, 1.6, 1.7, 1.8, 1.9$) using mechanical milling followed by annealing are explored. Temperature-dependent ^7Li spin-lattice relaxation NMR and MD simulations are combined to reveal the lithium ionic dynamics of lithium argyrodites. It is found that the lithium argyrodite with a composition of $\text{Li}_{5.7}\text{PS}_{4.7}\text{Cl}_{1.3}$ possesses the highest room temperature lithium ion conductivity of 6×10^{-3} S/cm. Finally, all-solid-state batteries with atomic layer deposition (ALD) LiNbO_3 -coated $\text{LiNi}_{0.8}\text{Mn}_{0.1}\text{Co}_{0.1}\text{O}_2$ cathode and In anode in combination with $\text{Li}_{5.7}\text{PS}_{4.7}\text{Cl}_{1.3}$ solid electrolyte are fabricated. EIS and GITT are used to further reveal the role of ALD LiNbO_3 coating layer.

2. Experimental

Reagent-grade Li_2S (99.98%, Sigma-Aldrich), P_2S_5 (99%, Sigma-Aldrich), and LiCl (99.0%, Sigma-Aldrich) crystalline powders were used as starting materials. The required amount of each starting material was calculated based on the composition $\text{Li}_{7-x}\text{PS}_{6-x}\text{Cl}_x$ ($x = 1.0, 1.1, 1.2, 1.3, 1.4, 1.5, 1.6, 1.7, 1.8, 1.9$) and then sealed in a ZrO_2 jar with 32 ZrO_2 balls ($16 \varphi = 10$ mm, $16 \varphi = 5$ mm) in an Argon filled glovebox (H_2O , $\text{O}_2 < 0.1$ ppm) due to the oxygen- and moisture-sensitive of the raw materials. The total weight of the starting mixture was almost 3.0 g. The details of the mechanical milling process can be found in previous work [20,22]. The obtained milled mixture was sealed in quartz tubes and annealed at various annealing conditions to obtain different annealed samples. $\text{Li}_{5.7}\text{PS}_{4.7}\text{Cl}_{1.3}$ with the highest ionic conductivity which was annealed at 350 °C for 15 h was chosen as the solid electrolyte for the all-solid-state batteries in this work.

Powder XRD patterns were collected over a 2θ range of 10–80° to identify the crystalline phases of the different samples using $\text{CuK}\alpha$ X-rays ($\lambda = 1.54178$ Å) on Bruker AXS D8. To prevent reaction with moisture and oxygen, the powders were sealed by Kapton foil in an Argon filled glove box. The ionic conductivity of the mixture annealed at various temperatures was determined by AC impedance spectroscopy. Stainless-steel disks and Indium foils were chosen as the blocking electrodes and attached on both faces of the 10 mm diameter powder pellet. AC impedance measurements were performed on the versatile multichannel potentiostat 3/Z (VMP3) in the frequency range of 1 Hz–7 MHz with an applied voltage of 0.02 V.

Solid-state NMR measurements were performed on a Varian Infinity Plus wide-bore NMR spectrometer equipped with an Oxford wide-bore magnet ($B_0 = 9.4$ T), operating at a ^7Li resonance frequency of 155.248 MHz. The $\pi/2$ pulse length was determined to be 2.3 μs . Chemical shifts were referenced with respect to a 1.0 M LiCl solution. The lithium argyrodites were sealed in custom-made Teflon tubes ($\varphi = 4.7$ mm) in an argon-filled glovebox (H_2O , $\text{O}_2 < 0.1$ ppm). Variable temperature measurements were performed using a 5 mm static probe. Spectra were recorded in the temperature range of 0–120 °C. The spin-lattice relaxation time T_1 was determined at various temperatures using a saturation recovery experiment.

AIMD simulations: We employed a $p(1 \times 1 \times 2)$ PBE functional optimized unit cell with stoichiometric $\text{Li}_6\text{PS}_5\text{Cl}$, $\text{Li}_{5.5}\text{PS}_{4.5}\text{Cl}_{1.5}$, $\text{Li}_5\text{PS}_4\text{Cl}_2$. All atoms were allowed to relax without constraints. The ab

initio molecular dynamic (AIMD) simulations were performed using the CP2K package [27]. All initial geometries that served as input for AIMD simulations were fully optimized to a local minimum by means of electronic-structure computations performed with CP2K. The generalized-gradient approximation in the parameterization of Perdew, Burke, and Ernzerhof (PBE) [28] was used to compute the exchange-correlation energy. The choice of the PBE functional is justified by its very good performance in describing bulk properties of main-group elements [29,30]. The valence electrons ($1s^25s^1$ for Li, $3s^23p^3$ for P, $3s^23p^4$ for S and $3s^23p^5$ for Cl) were described using hybrid Gaussian and plane-wave (GPW) basis sets [31], and the cutoff energy of 800 Rydberg of auxiliary plane wave basis sets was adopted. We employed special double- ζ valence plus polarization (DZVP) basis sets optimized to minimize basis set superposition errors [32]. Core electrons were described with scalar relativistic norm-conserving pseudopotentials [33]. Brillouin zone integration was performed with a reciprocal space mesh consisting of only the gamma point. In the simulations, we used Nose-Hoover thermostat (NVT) to sample from the canonical ensemble [34]. The relatively short time scales of AIMD (time step of 1.0 fs and total time of a simulation run of up to 60 ps) limit the sampling to fast and low-energy-barrier events. To rapidly explore a large phase space volume of surface configurations, a statistical sampling was performed at an elevated temperature of 800 K. All transition states (TSs) were determined by applying the nudged elastic band (NEB) method.

Laboratory-scale solid-state lithium batteries were prepared and cycled in this work. The bare $\text{LiNi}_{0.8}\text{Mn}_{0.1}\text{Co}_{0.1}\text{O}_2$ was from China Automotive Battery Research Institute and the LiNbO_3 -coated $\text{LiNi}_{0.8}\text{Mn}_{0.1}\text{Co}_{0.1}\text{O}_2$ was prepared by ALD according to our previous work [35]. The LiNbO_3 was deposited using a Savannah 100 ALD system (Veeco/carbon nanotube (CNT) division of the Veeco Instruments Inc.). Lithium tert-butoxide [$(\text{CH}_3)_3\text{COLi}$, Alfa Aesar, >99.9%] and niobium ethoxide [$\text{Nb}(\text{OEt})_5$, Et = $-\text{CH}_2\text{CH}_3$, Strem Chemicals Inc., >99.9%] were used for Li and Nb sources, respectively. Deionized water was used as the oxidant for both sub-cycles, and nitrogen was used as the carrier and purging gas. The deposition temperature for LiNbO_3 was performed at 235 °C. All the precursors were pulsed in for 1 s, followed by 15 s of nitrogen purge. For the cathode mixture used in solid-state lithium batteries, the $\text{Li}_{5.7}\text{PS}_{4.7}\text{Cl}_{1.3}$ was hand ground with bare $\text{LiNi}_{0.8}\text{Mn}_{0.1}\text{Co}_{0.1}\text{O}_2$ and LiNbO_3 -coated $\text{LiNi}_{0.8}\text{Mn}_{0.1}\text{Co}_{0.1}\text{O}_2$ with a weight ratio of 30:70 to obtain the final cathode mixtures, respectively. 10–11 mg of the above described cathode mixture was used in combination with 100 mg of $\text{Li}_{5.7}\text{PS}_{4.7}\text{Cl}_{1.3}$ electrolyte to make a 10 mm two-layer pellet by pressing. A pressure of 5 tons was applied to make the double-layer pellet followed by attaching a piece of In foil ($\varphi = 10$ mm) on the other side. Finally, the full solid-state battery pellet was pressed with 2 tons of pressure for 15 s. The assembled cell was charged and discharged applying various densities (0.255, 0.382, and 0.764 mA/cm^2) on LAND battery testing station under 1.88–3.78 V versus In (2.50–4.40 V vs. Li/Li^+) to evaluate the electrochemical performance. The galvanostatic intermittent titration technique (GITT) measurements were performed using a current density of 0.127 mA/cm^2 . The cyclic voltammetry (CV) measurements of those solid-state batteries were performed at 1.88–3.78 V vs. In with a sweep speed of 0.02 mV/s. Both the CV and EIS were performed on the versatile multichannel potentiostat 3/Z (VMP3). The obtained capacity in this work was normalized by the weight of the bare- and LiNbO_3 -coated $\text{LiNi}_{0.8}\text{Mn}_{0.1}\text{Co}_{0.1}\text{O}_2$ in the cathode mixture. All the electrochemical measurements for solid-state lithium batteries in this work are performed at room temperature.

3. Results and discussion

To investigate the optimal synthesis conditions for obtaining $\text{Li}_6\text{PS}_5\text{Cl}$ with the highest lithium ion conductivity, the ball milled pristine mixture was annealed at various temperatures (250, 300, 350, 400, 450, 500, and 550 °C) for 5 h. Fig. 1a shows the room temperature lithium ion conductivities of the annealed samples. The conductivity of

samples obtained after annealing at different temperatures are 6.11×10^{-4} S/cm for 250 °C, 9.37×10^{-4} S/cm for 300 °C, 9.18×10^{-4} S/cm for 350 °C, 1.12×10^{-3} S/cm for 400 °C, 1.07×10^{-3} S/cm for 450 °C, 9.98×10^{-4} S/cm for 500 °C, 1.62×10^{-3} S/cm for 550 °C, and 8.58×10^{-4} S/cm for 600 °C, respectively. The sample annealed at 550 °C shows the highest lithium ion conductivity. Moreover, the conductivities of the corresponding annealed samples shown in Fig. 1b also prove that 550 °C is the optimal annealing temperature when the heat treatment duration is fixed to 5 h. The annealed samples display much higher lithium ion conductivity than that of the mechanical milled mixture, showing that heat treatment is an effective route to improve the conductivity of lithium argyrodite. The corresponding activation energies deduced from the Arrhenius plot are 0.321 for 250 °C, 0.297 for 300 °C, 0.356 for 350 °C, 0.32 for 400 °C, 0.329 for 450 °C, 0.357 for 500 °C, and 0.296 for 550 °C, respectively. The high lithium ion conductivity of the maximum annealing temperature may be associated with the lowest activation energy. Rao et al. [36] have found that in order to reach a room temperature conductivity of 1 mS/cm and low activation energy of 0.16 eV, $\text{Li}_6\text{PS}_5\text{Cl}$ had to be heat-treated with a minimum temperature of 250 °C. The differences may come from the mechanical milling process. To explore the influence of annealing duration, the milled mixture was annealed at 550 °C for time periods of 3, 5, 8, and 10 h. As shown in Fig. 1c, the samples annealed for 8 h shows slightly higher lithium ion conductivities than that of samples annealed for different durations. In the inset of Fig. 1c, the room temperature lithium ion conductivities are 1.39×10^{-3} S/cm for 3 h, 1.62×10^{-3} S/cm for 5 h, 1.81×10^{-3} S/cm for 8 h, and 1.59×10^{-3} S/cm for 10 h, respectively. It should be noted that the sample annealed for 5 h shows the smallest activation energy,

which is not in good agreement with the changes in ionic conductivity. Previous research has shown that impedance spectroscopy results are highly dependent on the contacts between pellet and the blocking electrode [19]. To achieve good contact between the pellet and the blocking electrode, indium was chosen due to its inherent softness. For comparison, stainless steel was also used as the blocking electrode with the same $\text{Li}_6\text{PS}_5\text{Cl}$ (550 °C/8 h) material. As shown in Fig. 1c, the pellet using indium as the blocking electrode shows much higher lithium ion conductivity at various temperatures compared to that of stainless steel, suggesting that indium is a better blocking electrode for lithium argyrodite, which is also confirmed by the room temperature comparison in the inset of Fig. 1c.

MD simulations results have proved that introducing halogens into the argyrodite structure, which are distributed over the 4a and 4c sites, can effectively enhance the lithium ion conductivity [26]. Hereby, Cl was introduced into the $\text{Li}_6\text{PS}_5\text{Cl}$ structure to get $\text{Li}_{5.5}\text{PS}_{4.5}\text{Cl}_{1.5}$ with higher lithium ion conductivity. Fig. 1a shows the room temperature conductivity changes of annealed pristine mixtures which milled based on $\text{Li}_{5.5}\text{PS}_{4.5}\text{Cl}_{1.5}$. XRD patterns show that this material is a pure lithium argyrodite phase with a space group of $F-43m$. The room temperature conductivities are 2.96×10^{-4} S/cm for 150 °C, 8.03×10^{-4} S/cm for 200 °C, 1.47×10^{-4} S/cm for 250 °C, 2.05×10^{-3} S/cm for 300 °C, 3.07×10^{-3} S/cm for 350 °C, 2.17×10^{-3} S/cm for 400 °C, 1.35×10^{-3} S/cm for 500 °C, and 1.55×10^{-3} S/cm for 550 °C, respectively. The highest lithium ion conductivity was achieved when annealed at 350 °C for 5 h. This ionic conductivity is much higher than $\text{Li}_6\text{PS}_5\text{Cl}$, suggesting that introducing Cl is an effective way to enhance lithium ion conductivity in lithium argyrodite. Moreover, the Arrhenius plots in Fig. 1d also proved

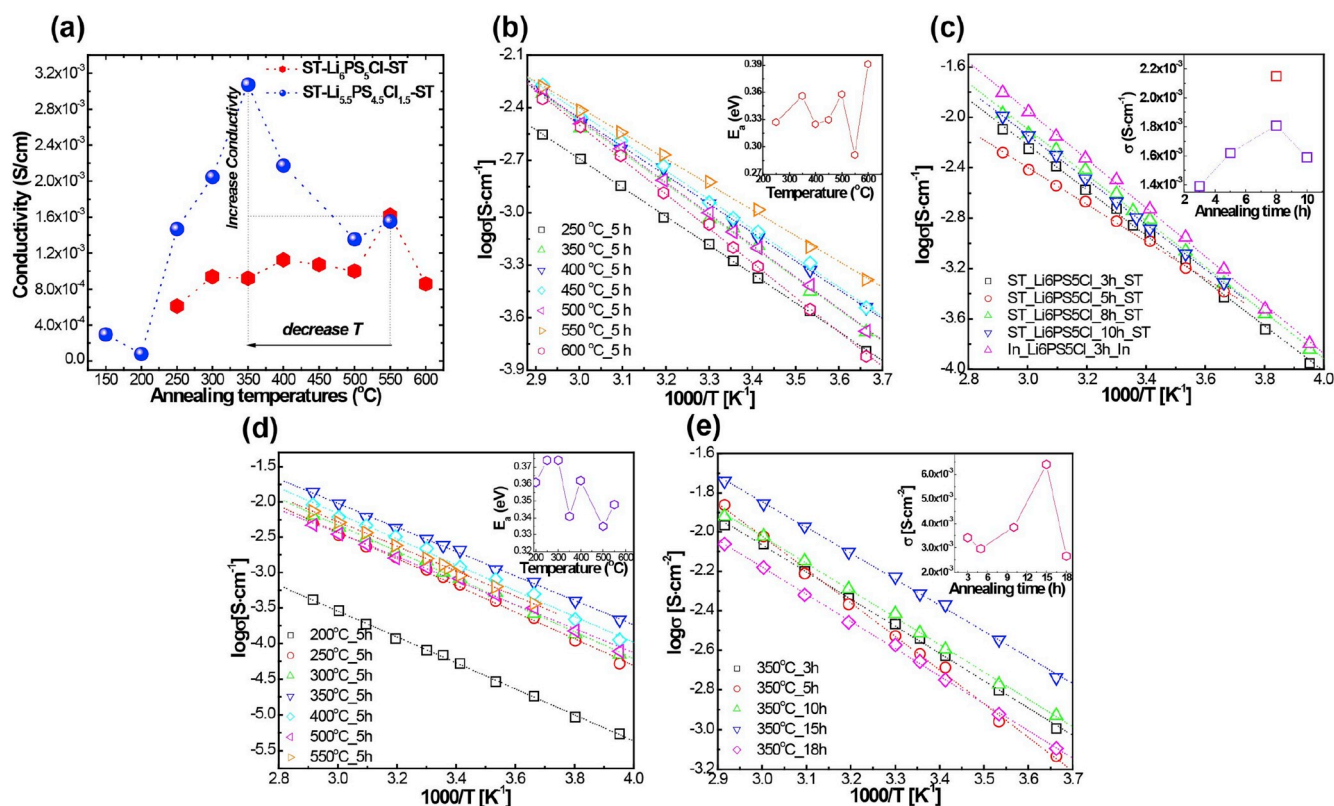


Fig. 1. (a) Room temperature Li-ion conductivity of $\text{Li}_6\text{PS}_5\text{Cl}$ and $\text{Li}_{5.5}\text{PS}_{4.5}\text{Cl}_{1.5}$ annealed at various temperatures. (b) The Arrhenius plots of the $\text{Li}_6\text{PS}_5\text{Cl}$ ball-milled mixture annealed at different temperatures for 5 h. The inset shows the corresponding activation energy changes as a function of annealing temperatures. (c) The Arrhenius plots of $\text{Li}_6\text{PS}_5\text{Cl}$ ball-milled precursor mixture annealed at 550 °C for various durations (3, 5, 8, and 10 h) using Stainless steel and indium foil as the blocking electrode, respectively. The inset figure is the room temperature lithium ion conductivities changes of $\text{Li}_6\text{PS}_5\text{Cl}$ annealed at various durations. (d) The Arrhenius plots of $\text{Li}_{5.5}\text{PS}_{4.5}\text{Cl}_{1.5}$ annealed at various temperatures for 5 h using stainless steel as the lithium ion blocking electrode. The inset shows the activation energy changes. (e) The Arrhenius plots of $\text{Li}_{5.5}\text{PS}_{4.5}\text{Cl}_{1.5}$ annealed at 350 °C for various durations: 3, 5, 10, 15, and 18 h. The inset shows the room temperature lithium ion conductivity changes.

that $\text{Li}_{5.5}\text{PS}_{4.5}\text{Cl}_{1.5}$ annealed at 350°C shows higher lithium ion conductivity at various temperatures than that of other heat-treated temperatures. Fig. 1e shows the room temperature conductivity for $\text{Li}_{5.5}\text{PS}_{4.5}\text{Cl}_{1.5}$ annealed at 350°C for various durations (3, 5, 10, 15, 18 h). The corresponding lithium ion conductivity are 3.68×10^{-3} S/cm for 3 h, 3.46×10^{-3} S/cm for 5 h, 3.84×10^{-3} S/cm for 10 h, 6.41×10^{-3} S/cm for 15 h, and 2.76×10^{-3} S/cm for 18 h, respectively. The corresponding activation energies deduced from the Arrhenius plots, are 0.272 eV for 3 h, 0.248 eV for 5 h, 0.273 eV for 10 h, 0.261 eV for 15 h, and 0.273 for 18 h, respectively. The activation energies of $\text{Li}_{5.5}\text{PS}_{4.5}\text{Cl}_{1.5}$ annealed at 350°C show smaller values than that of $\text{Li}_6\text{PS}_5\text{Cl}$, which is due to a large number of Li vacancies caused by Cl doping. The introducing Cl in the structure provides many Li vacancies distributed among the framework. The electrostatic force between Li–Li interaction in $\text{Li}_{5.5}\text{PS}_{4.5}\text{Cl}_{1.5}$ decreases due to the exist of Li vacancies. Fast lithium ion conduction can be achieved for $\text{Li}_{5.5}\text{PS}_{4.5}\text{Cl}_{1.5}$ by hopping the mobile lithium ions through these introduced lithium vacancies on the equivalent (or nearly equivalent) sites, yielding a ultrafast lithium ion diffusion and smaller energy barrier [7]. This is in good agreement with the simulated predictions [26]. Another possible reason may associated with the disorder of S/Cl over the 4a and 4c sites after the introduction of Cl in $\text{Li}_6\text{PS}_5\text{Cl}$. The limiting jump rate in $\text{Li}_6\text{PS}_5\text{Cl}$ is the doublet or inter-cage jumps, which depends on the Cl ordering over 4a and 4c sites [1,21,26]. However, due to the similar X-ray scatter factor of Cl and S, it is impossible to detect S/Cl disorder by XRD, power neutron diffraction is needed.

Fig. 2a shows the Arrhenius plots of pristine and annealed $\text{Li}_6\text{PS}_5\text{Cl}$

and $\text{Li}_{5.5}\text{PS}_{4.5}\text{Cl}_{1.5}$ using stainless steel and indium as the blocking electrode, respectively. The milled $\text{Li}_6\text{PS}_5\text{Cl}$ shows higher lithium ionic conductivities than $\text{Li}_{5.5}\text{PS}_{4.5}\text{Cl}_{1.5}$ at different temperatures. Previous research has shown that the pure lithium argyrodite phase can be formed during the high-energy mechanical milling process [20,22]. However, this process is highly dependent on the milling apparatus and the total weight ration of balls and starting materials. In this work, due to the apparatus limitation, pure lithium argyrodite cannot be synthesized by direct mechanical milling. For the milling mixture of $\text{Li}_{5.5}\text{PS}_{4.5}\text{Cl}_{1.5}$, additional LiCl was introduced and caused lower lithium ion conductivity. As shown by the data of annealed samples in Fig. 2a, $\text{Li}_{5.5}\text{PS}_{4.5}\text{Cl}_{1.5}$ shows higher lithium ion conductivity than $\text{Li}_6\text{PS}_5\text{Cl}$ using both stainless steel and indium as blocking electrodes, suggesting that superionic ionic conductivity can be achieved by introducing Cl to tailor S/Cl disorder in the structure. Additionally, the activation energy deduced from temperature-dependent ionic conductivity measurements is decreased by introducing Cl in the structure. Unlike AC impedance which is highly influenced by the pellet morphology and contacts with blocking electrode, solid-state NMR is a powerful tool to probe the lithium mobility in a short diffusion length [1,2,21]. To double clarify the lithium jump rates of $\text{Li}_6\text{PS}_5\text{Cl}$ and $\text{Li}_{5.5}\text{PS}_{4.5}\text{Cl}_{1.5}$, ^7Li spin-lattice relaxation (SLR) rates as a function of temperatures were performed on both samples, as shown in Fig. 2b. The β values of $\text{Li}_6\text{PS}_5\text{Cl}$ and $\text{Li}_{5.5}\text{PS}_{4.5}\text{Cl}_{1.5}$ are 1.45 and 1.67, which are similar to what was observed for lithium argyrodite [1,2,19,20,37,38], suggesting a 3D diffusion process for lithium ions in our samples. At extremely low temperatures, the longitudinal relaxation is primarily induced by lattice vibrations or

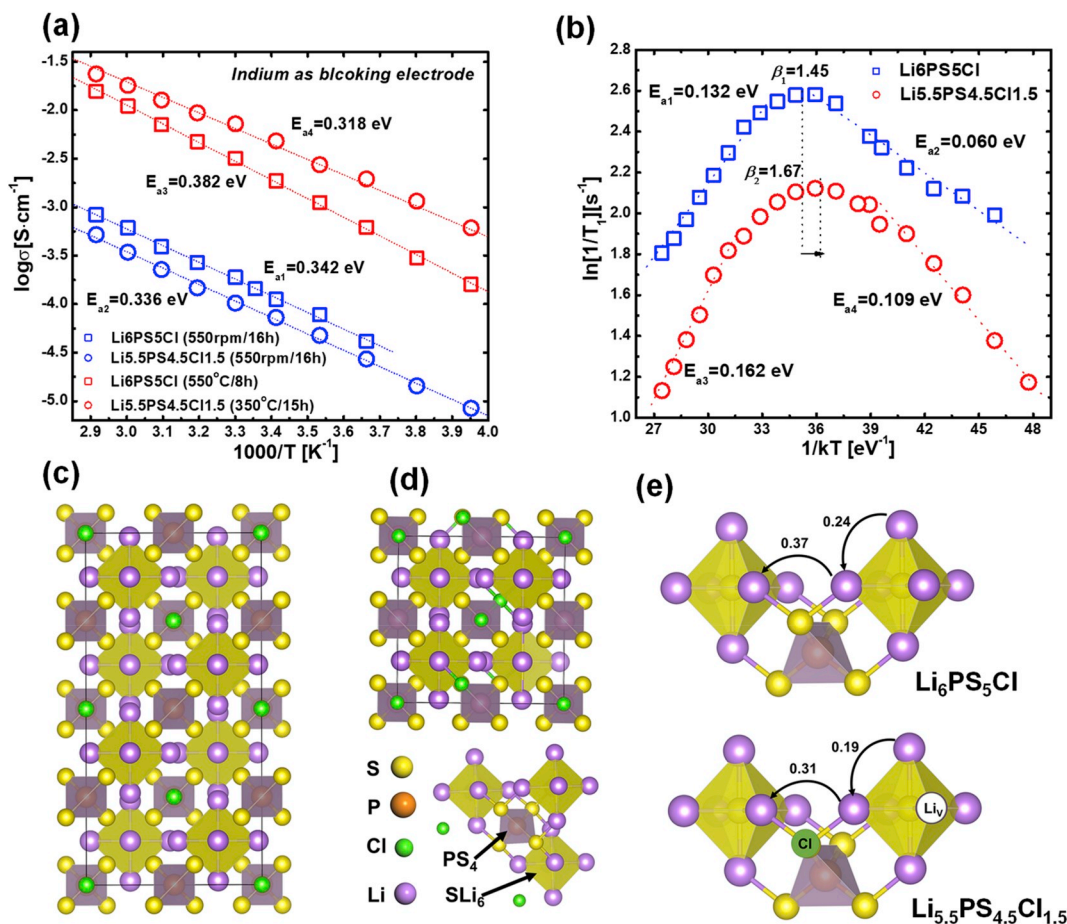


Fig. 2. (a) The Arrhenius plots of ball milled $\text{Li}_6\text{PS}_5\text{Cl}$ and $\text{Li}_{5.5}\text{PS}_{4.5}\text{Cl}_{1.5}$ (550 rpm/16 h), annealed ($550^\circ\text{C}/8$ h) and $\text{Li}_{5.5}\text{PS}_{4.5}\text{Cl}_{1.5}$ ($350^\circ\text{C}/15$ h) using indium as the blocking electrode. (b) Temperature-dependent ^7Li spin-lattice relaxation (SLR) NMR rates for annealed $\text{Li}_6\text{PS}_5\text{Cl}$ and $\text{Li}_{5.5}\text{PS}_{4.5}\text{Cl}_{1.5}$ samples measured in the laboratory frame of the reference. The Larmor frequency is 155.248 MHz. Crystal structure of $\text{Li}_6\text{PS}_5\text{Cl}$ (c) and $\text{Li}_{5.5}\text{PS}_{4.5}\text{Cl}_{1.5}$ (d). (e) The energy barrier for lithium ion migration in $\text{Li}_6\text{PS}_5\text{Cl}$ (up) and $\text{Li}_{5.5}\text{PS}_{4.5}\text{Cl}_{1.5}$ (down) from ab initio molecular dynamics (AIMD) simulations.

coupling of the Li spins ($I = 3/2$) with paramagnetic impurities [39], while in this work the SLR rates have not been probed at such low-temperature flank due to the experimental limitation. At high-temperature flank, the range we chose in this work, the spin-lattice relaxation rates intensely increase with temperature until characteristic diffusion-induced SLR rates peaks appear for both $\text{Li}_6\text{PS}_5\text{Cl}$ and $\text{Li}_{5.5}\text{PS}_{4.5}\text{Cl}_{1.5}$ as shown in Fig. 2b. This confirms that the spin-lattice relaxation behavior in both samples are induced by Li self-diffusion in the temperature range [39]. The lithium ion jumps frequency and the corresponding energy barrier can be quantified from the temperature dependence of ^7Li SLR rates in the laboratory frame (the Larmor frequency). The hopping frequency is given by τ^{-1} , where τ is the average residence time between the subsequent jumps. When the hopping frequency is in the order of the Larmor frequency (ω_0), $1/T_1$ reaches the maximum as a function of temperature, indicating the maximum transfer of energy toward the Li-ion nuclear spin. When the maximum relaxation rate ($1/T_1$) reaches, an absolute lithium jump rate can be calculated based on the maximum condition $\tau \cdot \omega_0 \approx 1$ [1,19]. Since $\text{Li}_6\text{PS}_5\text{Cl}$ and $\text{Li}_{5.5}\text{PS}_{4.5}\text{Cl}_{1.5}$ were probed with the same Larmor frequency (155.248 MHz), they should have the same lithium diffusion coefficient based on the assumption that the diffusion length is the same. As shown in Fig. 2b, the maximum SLR rate is reached at 328 K for $\text{Li}_6\text{PS}_5\text{Cl}$ and at 320 K for $\text{Li}_{5.5}\text{PS}_{4.5}\text{Cl}_{1.5}$, respectively. $\text{Li}_{5.5}\text{PS}_{4.5}\text{Cl}_{1.5}$ displays the same lithium jump rate at a lower temperature compared to $\text{Li}_6\text{PS}_5\text{Cl}$, suggesting that $\text{Li}_{5.5}\text{PS}_{4.5}\text{Cl}_{1.5}$ has a faster lithium mobility than that of $\text{Li}_6\text{PS}_5\text{Cl}$. The residence time τ show typical Arrhenius behavior, thus the slopes of the low- and high-temperature flank of the SLR rate can be used to deduce the activation energies for short- and long-range lithium ion diffusional processes in lithium argyrodite, respectively [1,19,20,37]. The activation energies deduced from the high- and low-temperature flanks of $\text{Li}_6\text{PS}_5\text{Cl}$ are 0.132 and 0.060 eV, while the corresponding values of $\text{Li}_{5.5}\text{PS}_{4.5}\text{Cl}_{1.5}$ are 0.162 and 0.109 eV, respectively. Fig. 2(c) and (d) show the energy barrier for lithium ion migration in $\text{Li}_6\text{PS}_5\text{Cl}$ and $\text{Li}_{5.5}\text{PS}_{4.5}\text{Cl}_{1.5}$ based on the AIMD simulations

results. The energy barriers for lithium ions migration from the 48h site to the nearest neighbor 48h site in the Li_6S group for $\text{Li}_6\text{PS}_5\text{Cl}$ and $\text{Li}_{5.5}\text{PS}_{4.5}\text{Cl}_{1.5}$ are 0.24 and 0.19 eV, while the corresponding energy barriers for lithium ions move from one Li_6S group to the nearest neighbor Li_6S are much larger, 0.37 and 0.31 eV. $\text{Li}_{5.5}\text{PS}_{4.5}\text{Cl}_{1.5}$ shows small energy barriers values than that of $\text{Li}_6\text{PS}_5\text{Cl}$ in both short or long diffusion length scales. The AIMD simulations results show that introducing Cl in the PS_4 group can effectively decrease the energy barrier for lithium ion migration, thus promoting lithium ion diffusion in $\text{Li}_{5.5}\text{PS}_{4.5}\text{Cl}_{1.5}$. However, these values are slightly larger than the activation energies deduced from the high-temperature flanks. That is because the high complexity of the lithium diffusion process makes an underestimation of the activation energy for the bulk diffusion from SLR NMR results.

Since introducing Cl in the $\text{Li}_6\text{PS}_5\text{Cl}$ to form $\text{Li}_{5.5}\text{PS}_{4.5}\text{Cl}_{1.5}$ is an effective route to promote lithium ion conductivity, $\text{Li}_{7-x}\text{PS}_{6-x}\text{Cl}_x$ ($x = 1.1, 1.2, 1.3, 1.4, 1.5, 1.6, 1.7, 1.8, \text{ and } 1.9$) was systematically investigated. Two annealing temperatures, 350 and 500 °C were chosen and the annealing duration was fixed to 15 h to prepare the lithium argyrodites. Fig. 3a shows the XRD patterns for mixtures with different composition prepared by mechanically milling of Li_2S , P_2S_5 , and LiCl powder at 550 rpm for 16 h, and then annealed at 350 °C for 15 h. XRD patterns show that the major diffraction reflections belong to lithium argyrodite were detected for low Cl amount samples, $\text{Li}_{7-x}\text{PS}_{6-x}\text{Cl}_x$ ($x = 1.1, 1.2, 1.3, 1.4, 1.5, 1.6$), suggesting that pure lithium argyrodite can be synthesized at low annealing temperature when a low amount of Cl was introduced in $\text{Li}_6\text{PS}_5\text{Cl}$ structure. Meanwhile, very weak lithium argyrodite diffraction peaks were observed in the patterns of samples with high Cl content ($\text{Li}_{7-x}\text{PS}_{6-x}\text{Cl}_x$ ($x = 1.1, 1.2, 1.3, 1.4, 1.5, 1.6$)), showing that an annealing temperature of 350 °C is not high enough to get pure lithium argyrodite. Therefore, the annealing temperature was increased to 500 °C and the annealing time was fixed to 15 h. Fig. 3b displays the XRD patterns of the mixtures with different compositions annealed at 500 °C for 10 h. All of the major diffraction peaks of the

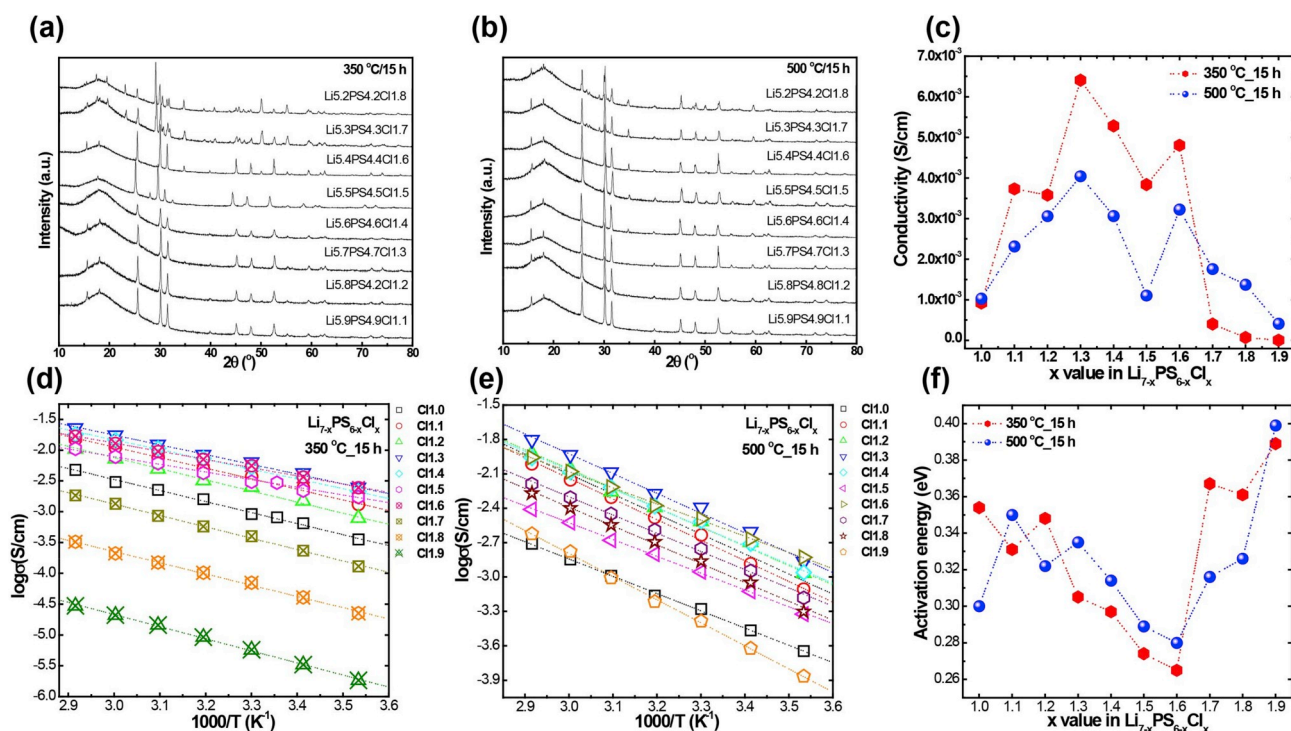


Fig. 3. XRD patterns of the $\text{Li}_{7-x}\text{PS}_{6-x}\text{Cl}_x$ ($x = 1.1, 1.2, 1.3, 1.4, 1.5, 1.6, 1.7, 1.8$) ball milled pristine precursor mixture annealed at (a) 350 °C and (b) 500 °C for 15 h. (c) Room temperature lithium ion conductivity of $\text{Li}_{7-x}\text{PS}_{6-x}\text{Cl}_x$ ($x = 1.0, 1.1, 1.2, 1.3, 1.4, 1.5, 1.6, 1.7, 1.8, 1.9$) annealed at 350 and 500 °C for 15 h. (d, e) The corresponding Arrhenius plots of different lithium argyrodites annealed at different temperatures. (f) The activation energy changes of $\text{Li}_{7-x}\text{PS}_{6-x}\text{Cl}_x$ ($x = 1.0, 1.1, 1.2, 1.3, 1.4, 1.5, 1.6, 1.7, 1.8, 1.9$) annealed at 350 and 500 °C for 15 h.

patterns for $\text{Li}_{7-x}\text{PS}_{6-x}\text{Cl}_x$ ($x = 1.1, 1.2, 1.3, 1.4, 1.5, 1.6, 1.7, 1.8$) can be indexed to the $\text{Li}_6\text{PS}_5\text{Cl}$ crystal structure, although several weak additional reflections are still visible for $\text{Li}_{7-x}\text{PS}_{6-x}\text{Cl}_x$ ($x = 1.4, 1.5, 1.6, 1.7, 1.8$) at $2\theta = 29^\circ, 35^\circ$ and 51° , which belongs to the diffraction peaks of the starting material LiCl . Fig. 3c shows room temperature lithium ionic conductivities of $\text{Li}_{7-x}\text{PS}_{6-x}\text{Cl}_x$ ($x = 1.0, 1.1, 1.2, 1.3, 1.4, 1.5, 1.6, 1.7, 1.8, 1.9$) annealed at 350 and 500 °C for 15 h. When an annealing temperature of 350 °C was chosen, the room temperature lithium ionic conductivities for these different compositions were found to be 9.17×10^{-4} S/cm for $\text{Li}_6\text{PS}_5\text{Cl}$, 3.73×10^{-3} S/cm for $\text{Li}_{5.9}\text{PS}_{4.9}\text{Cl}_{1.1}$, 3.58×10^{-3} S/cm for $\text{Li}_{5.8}\text{PS}_{4.8}\text{Cl}_{1.2}$, 6.41×10^{-3} S/cm for $\text{Li}_{5.7}\text{PS}_{4.7}\text{Cl}_{1.3}$, 5.28×10^{-3} S/cm for $\text{Li}_{5.6}\text{PS}_{4.6}\text{Cl}_{1.4}$, 3.84×10^{-3} S/cm for $\text{Li}_{5.5}\text{PS}_{4.5}\text{Cl}_{1.5}$, 4.81×10^{-3} S/cm for $\text{Li}_{5.4}\text{PS}_{4.4}\text{Cl}_{1.6}$, 4.01×10^{-4} S/cm for $\text{Li}_{5.3}\text{PS}_{4.3}\text{Cl}_{1.7}$, 7.02×10^{-5} S/cm for $\text{Li}_{5.2}\text{PS}_{4.2}\text{Cl}_{1.8}$, and 5.75×10^{-6} S/cm for $\text{Li}_{5.1}\text{PS}_{4.1}\text{Cl}_{1.9}$, respectively. The composition $\text{Li}_{5.7}\text{PS}_{4.7}\text{Cl}_{1.3}$ displayed a much higher room temperature lithium ion conductivity than that of other compositions. When the annealing temperature was increased to 500 °C, the corresponding room temperature lithium ionic conductivities are 1.03×10^{-3} S/cm for $\text{Li}_6\text{PS}_5\text{Cl}$, 2.32×10^{-3} S/cm for $\text{Li}_{5.9}\text{PS}_{4.9}\text{Cl}_{1.1}$, 3.06×10^{-3} S/cm for $\text{Li}_{5.8}\text{PS}_{4.8}\text{Cl}_{1.2}$, 4.04×10^{-3} S/cm for $\text{Li}_{5.7}\text{PS}_{4.7}\text{Cl}_{1.3}$, 3.06×10^{-3} S/cm for $\text{Li}_{5.6}\text{PS}_{4.6}\text{Cl}_{1.4}$, 1.11×10^{-3} S/cm for $\text{Li}_{5.5}\text{PS}_{4.5}\text{Cl}_{1.5}$, 3.23×10^{-3} S/cm for $\text{Li}_{5.4}\text{PS}_{4.4}\text{Cl}_{1.6}$, 1.76×10^{-3} S/cm for $\text{Li}_{5.3}\text{PS}_{4.3}\text{Cl}_{1.7}$, 1.37×10^{-3} S/cm for $\text{Li}_{5.2}\text{PS}_{4.2}\text{Cl}_{1.8}$, and 6.13×10^{-4} S/cm for $\text{Li}_{5.1}\text{PS}_{4.1}\text{Cl}_{1.9}$, respectively. At higher annealing temperature (500 °C), $\text{Li}_6\text{PS}_5\text{Cl}$, $\text{Li}_{5.3}\text{PS}_{4.3}\text{Cl}_{1.7}$, $\text{Li}_{5.2}\text{PS}_{4.2}\text{Cl}_{1.8}$, and $\text{Li}_{5.1}\text{PS}_{4.1}\text{Cl}_{1.9}$ show enhanced lithium ionic conductivities compared to that of samples annealed at lower annealing temperature (350 °C). It can be concluded that introducing Cl in the structure can not only promoting the ionic conductivity but also can decrease the annealing temperature required to obtain pure lithium argyrodite for $\text{Li}_6\text{PS}_5\text{Cl}$. However, the introduction of too much Cl into the structure will decrease lithium ion conductivity due to the existence of LiCl in the annealed sample which will impede lithium ion conduction. The temperature-dependent conductivities of $\text{Li}_{7-x}\text{PS}_{6-x}\text{Cl}_x$ ($x = 1.0, 1.1, 1.2, 1.3, 1.4, 1.5, 1.6, 1.7, 1.8, 1.9$) annealed at 350 and 500 °C are shown in Fig. 3d and e. At 350 °C, $\text{Li}_{7-x}\text{PS}_{6-x}\text{Cl}_x$ ($x = 1.1, 1.2, 1.3, 1.4, 1.5, 1.6$) show much higher lithium ionic conductivities at different measuring temperatures than that of $\text{Li}_6\text{PS}_5\text{Cl}$, while $\text{Li}_{7-x}\text{PS}_{6-x}\text{Cl}_x$ ($x = 1.7, 1.8, 1.9$) display lower values, which is in good agreement with the lithium ionic conductivities changes at room temperature for different compositions. At the higher annealing temperature (500 °C), introducing of Cl in the structure can improve the lithium ion conductivity at various temperatures for most compositions except for $\text{Li}_{5.1}\text{PS}_{4.1}\text{Cl}_{1.9}$. The activation energies deduced

from the temperature-dependent impedance spectroscopy for $\text{Li}_{7-x}\text{PS}_{6-x}\text{Cl}_x$ ($x = 1.0, 1.1, 1.2, 1.3, 1.4, 1.5, 1.6, 1.7, 1.8, 1.9$) annealed at 350 and 500 °C are shown in Fig. 3f. For $\text{Li}_{5.7}\text{PS}_{4.7}\text{Cl}_{1.3}$, $\text{Li}_{5.6}\text{PS}_{4.6}\text{Cl}_{1.4}$, $\text{Li}_{5.5}\text{PS}_{4.5}\text{Cl}_{1.5}$, and $\text{Li}_{5.4}\text{PS}_{4.4}\text{Cl}_{1.6}$, the lower annealing temperature (350 °C) yielded smaller activation energies than that at higher annealing temperature (500 °C), which may be associated with higher lithium ion conductivities. While for high Cl doping amount, $\text{Li}_{5.3}\text{PS}_{4.3}\text{Cl}_{1.7}$ and $\text{Li}_{5.2}\text{PS}_{4.2}\text{Cl}_{1.8}$ show smaller activation energies values when the annealing temperature was 500 °C, which is in good agreement with the conductivity changes.

To further confirm the optimal composition with the highest lithium ion conductivity among $\text{Li}_{7-x}\text{PS}_{6-x}\text{Cl}_x$ ($x = 1.1, 1.2, 1.3, 1.4, 1.6, \text{ and } 1.7$), temperature-dependent ^7Li SLR NMR were performed to quantify the bulk diffusion behavior. As shown in Fig. 4(a) for the SLR rate curves of $\text{Li}_{7-x}\text{PS}_{6-x}\text{Cl}_x$ ($x = 1.1, 1.2, 1.3, 1.4, 1.6, \text{ and } 1.7$), the maxima were achieved for each of the relaxation curves in the measured temperature range in this work and the corresponding temperatures are plotted and shown in Fig. 4(b). The β values for each curve were calculated based on the activation energies deduced from the low- and high-temperature flanks. As shown in Fig. 4(b), the β values are in the range between 1 and 2, indicating that the underlying hopping correlation function is represented by a non-exponential rather than an exponential function [40]. $\text{Li}_{5.7}\text{PS}_{4.7}\text{Cl}_{1.3}$ shows the lowest temperature corresponding to the maxima, suggesting the highest lithium diffusion in the bulk among all of these various compositions [1,19,20,37]. Previous research has shown that the activation energy deduced from the high-temperature flank is representative for the “bulk” or long-range Li-ion diffusion in the structure [1,38]. The corresponding activation energies here are 0.174 eV for $\text{Li}_{5.9}\text{PS}_{4.9}\text{Cl}_{1.1}$, 0.138 eV for $\text{Li}_{5.8}\text{PS}_{4.8}\text{Cl}_{1.2}$, 0.182 eV for $\text{Li}_{5.7}\text{PS}_{4.7}\text{Cl}_{1.3}$, 0.147 eV for $\text{Li}_{5.6}\text{PS}_{4.6}\text{Cl}_{1.4}$, 0.145 eV for $\text{Li}_{5.4}\text{PS}_{4.4}\text{Cl}_{1.6}$, and 0.134 eV for $\text{Li}_{5.3}\text{PS}_{4.3}\text{Cl}_{1.7}$, respectively. However, as shown in Fig. 3(f), the activation energies deduced from the temperature-dependent impedance spectroscopy are 0.331 eV for $\text{Li}_{5.9}\text{PS}_{4.9}\text{Cl}_{1.1}$, 0.348 eV for $\text{Li}_{5.8}\text{PS}_{4.8}\text{Cl}_{1.2}$, 0.305 eV for $\text{Li}_{5.7}\text{PS}_{4.7}\text{Cl}_{1.3}$, 0.297 eV for $\text{Li}_{5.6}\text{PS}_{4.6}\text{Cl}_{1.4}$, 0.265 eV for $\text{Li}_{5.4}\text{PS}_{4.4}\text{Cl}_{1.6}$, and 0.367 eV for $\text{Li}_{5.3}\text{PS}_{4.3}\text{Cl}_{1.7}$, respectively. All of these activation energies obtained from the slope of high-temperature flanks for different compositions are lower than that obtained from the temperature-dependent impedance. This result is because the energy barrier obtained from AC impedance spectroscopy reflects the contribution from both the bulk and the grain boundaries parts, while NMR probes a much short diffusion length scales, such as the back-and-forth jumps and/or intracage jumps in lithium argyrodites [1,37,41]. Another thing that should be noted is that

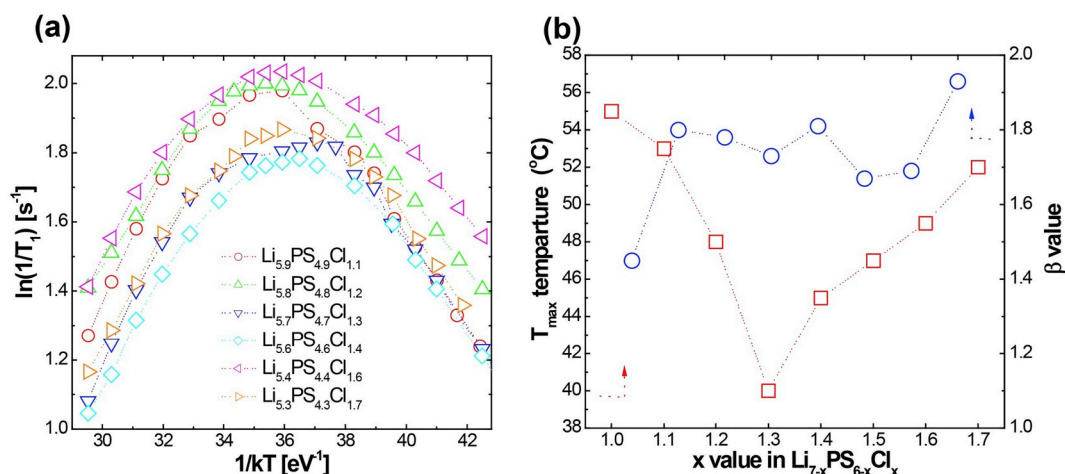


Fig. 4. (a) ^7Li spin-lattice relaxation rates of $\text{Li}_{7-x}\text{PS}_{6-x}\text{Cl}_x$ ($x = 1.1, 1.2, 1.3, 1.4, 1.6, \text{ and } 1.7$) annealed at 350 °C for 10 h as a function of reciprocal temperatures measured at the same field strengths (9.4 T). (b) The corresponding value of T_{\max} and β obtained from the temperature dependent ^7Li SLR rates plot. (c) The corresponding activation energies of different lithium argyrodites obtained from the high- and low-temperature flank by an Arrhenius fit, which represent the long- and short-range diffusion processes, respectively.

$\text{Li}_{5.8}\text{PS}_{4.8}\text{Cl}_{1.2}$ and $\text{Li}_{5.3}\text{PS}_{4.3}\text{Cl}_{1.7}$ similarly show smaller activation energies from the high-temperature flank compared to other compositions, while the lithium ionic conductivities of which are quite small among these compositions. Conversely, $\text{Li}_{5.7}\text{PS}_{4.7}\text{Cl}_{1.3}$ with the highest lithium ion conductivity shows the largest activation energies from the high-temperature SLR flank. A similar situation is also observed when looking at the changes in activation energies obtained from impedance spectroscopy. The macroscopic diffusion of lithium ion lithium argyrodite needs the combination of these three kinds of jumps, i.e., the 48h–48h jump, the intra-cage jump, and the inter-cage jump [1]. The high complexity of lithium diffusion process in lithium argyrodite structure may lead to a broadening of the hopping induced spectral density, thus yielded an underestimation of the activation energy to bulk diffusion as derived from the high-temperature flank of SLR NMR [37]. That is to say, for $\text{Li}_{7-x}\text{PS}_{6-x}\text{Cl}_x$ ($x = 1.1, 1.2, 1.3, 1.4, 1.6, 1.7, 1.8,$ and 1.9), the activation energies deduced from temperature-dependent AC impedance and SLR NMR are not the only parameter to estimate the lithium ion conductivity.

Previous research has proven that a decomposition effect occurs at the interface of the sulfide-based solid electrolyte and carbon additive [21,42,43], where the side products of which would restrict the conduction of electron and/or lithium ions in the cathode composite. To avoid the side reaction between the solid electrolyte and carbon

interface in the cathode, a special cathode composite without carbon was designed and applied in solid-state lithium batteries. The cathode composite was made by hand grounding $\text{Li}_{5.7}\text{PS}_{4.7}\text{Cl}_{1.3}$ (or $\text{Li}_6\text{PS}_5\text{Cl}$) and the active materials with a weight ratio of 30/70. The assembled all-solid-state lithium batteries were cycled at various current densities ($0.255, 0.382,$ and 0.764 mA/cm^2) between 1.88 and 3.78 V versus In ($2.50\text{--}4.40 \text{ V vs. Li/Li}^+$), the results of which are shown in Fig. 5(a–f). The initial charge capacities for solid-state lithium batteries using bare $\text{LiNi}_{0.8}\text{Mn}_{0.1}\text{Co}_{0.1}\text{O}_2$ as active material cycled at 200, 300, and 600 μA , corresponding to the current density of 0.255, 0.382, and 0.764 mA/cm^2 , respectively, are 140.0, 115.8, and 104 mAh/g. The initial Coulombic efficiencies are 66.63%, 62.71%, and 63.08%. The low Coulombic efficiencies may be associated with the In anode. After the deinsertion of lithium ions from the cathode layer material, part of these lithium ions is inserted in the anode material to form lithium indium alloy compounds. LiNbO_3 is an effective buffer layer to reduce the interfacial resistance and improve the electrochemical performances of cathode materials [44,45]. After coating the $\text{LiNi}_{0.8}\text{Mn}_{0.1}\text{Co}_{0.1}\text{O}_2$ with LiNbO_3 using ALD, the initial discharge capacity at the same current densities are 140.8, 121.3, and 95.4 mAh/g, with the corresponding Coulombic efficiencies of 65.12%, 61.03%, and 66.98%, respectively. It is interesting to note that the LiNbO_3 -coating has a negligible effect on the initial discharge capacity and the initial Coulombic efficiency.

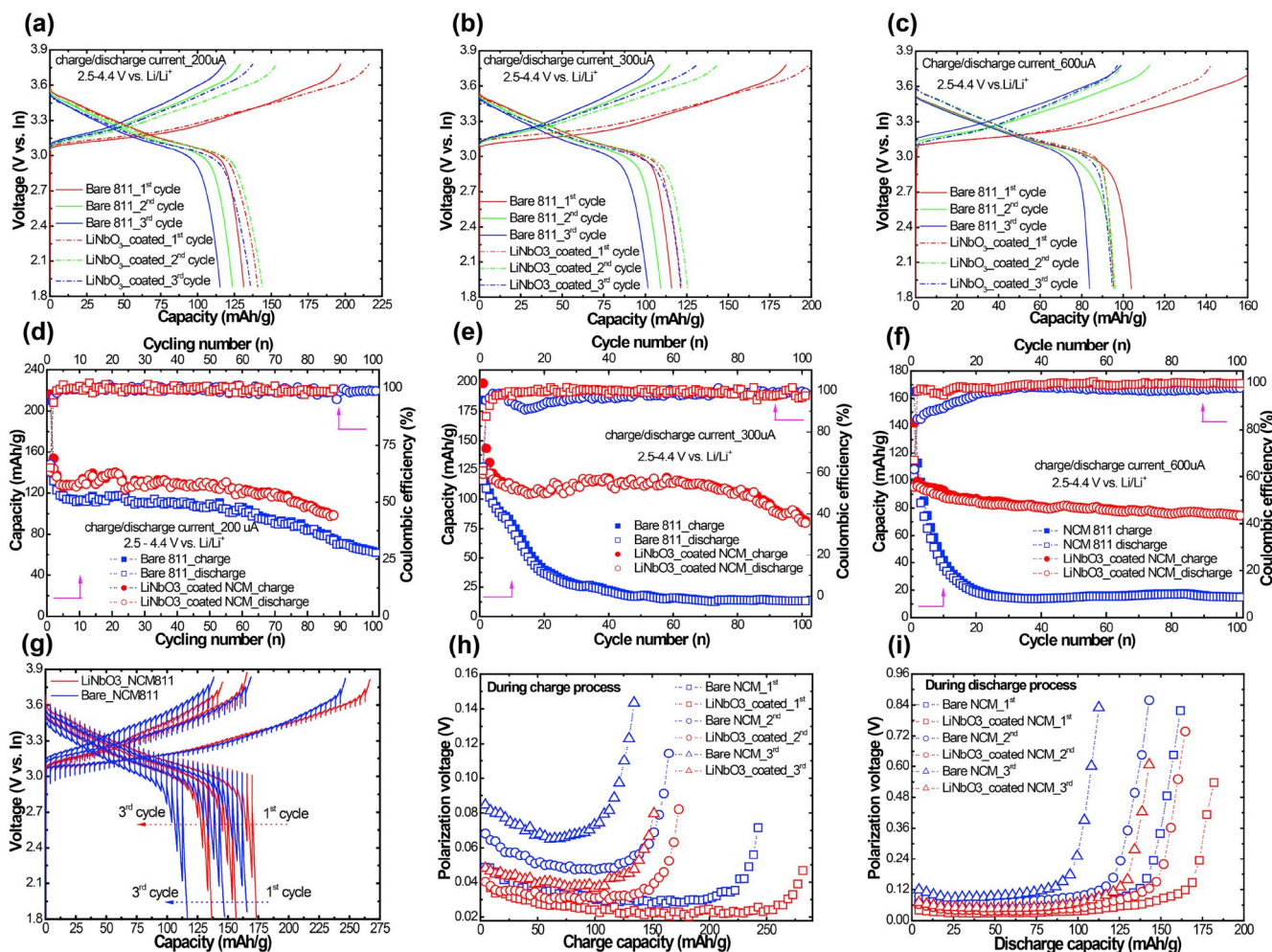


Fig. 5. Galvanostatic voltage curves for the first three cycles of the solid-state Li batteries using bare $\text{LiNi}_{0.8}\text{Mn}_{0.1}\text{Co}_{0.1}\text{O}_2$ and LiNbO_3 -coated $\text{LiNi}_{0.8}\text{Mn}_{0.1}\text{Co}_{0.1}\text{O}_2$ as cathode materials in combination with $\text{Li}_{5.7}\text{PS}_{4.7}\text{Cl}_{1.3}$ solid electrolyte and In anode at different charge/discharge currents: (a) 200 μA , (b) 300 μA , (c) 600 μA between 1.88 and 3.78 V vs. In ($2.5\text{--}4.4 \text{ V vs. Li/Li}^+$). The solid and dashed/dotted lines represent solid-state batteries using bare and LiNbO_3 -coated $\text{LiNi}_{0.8}\text{Mn}_{0.1}\text{Co}_{0.1}\text{O}_2$ cathode materials, respectively. The corresponding capacity retention and Coulombic efficiency changes during the first 100 cycles (d, e, f). (g) GITT curves of solid-state lithium batteries using bare $\text{LiNi}_{0.8}\text{Mn}_{0.1}\text{Co}_{0.1}\text{O}_2$ (blue line) and LiNbO_3 -coated $\text{LiNi}_{0.8}\text{Mn}_{0.1}\text{Co}_{0.1}\text{O}_2$ (red line) as cathode materials in the first three cycles at a rate of 0.1C. The corresponding polarization plots obtained by GITT during the charge (h) and discharge processes (i).

However, after two cycles, the discharge capacities of the LiNbO_3 -coated battery are 135.9, 121.7, and 94.7 mAh/g, which are higher than the bare $\text{LiNi}_{0.8}\text{Mn}_{0.1}\text{Co}_{0.1}\text{O}_2$ battery (131.8, 101.7, and 83.8 mAh/g, respectively). For comparison, the initial charge and discharge capacities for the LiNbO_3 -coated battery using $\text{Li}_6\text{PS}_5\text{Cl}$ as solid electrolyte and In foil as anode cycled under 200 μA at the same charge/discharge voltage window are 147.7 and 96.0 mAh/g with an initial coulombic efficiency of 64.96%, as shown in Fig. S1(a). Both the initial charge/discharge capacities and the corresponding coulombic efficiency are smaller than that of solid-state battery using $\text{Li}_{5.7}\text{PS}_{4.7}\text{Cl}_{1.3}$ as solid electrolyte, which are due to the higher lithium ion conductivity of $\text{Li}_{5.7}\text{PS}_{4.7}\text{Cl}_{1.3}$ solid electrolyte. Fig. 5(d–f) show the capacity retention during the first 100 cycles at various current densities of solid-state batteries using $\text{Li}_{5.7}\text{PS}_{4.7}\text{Cl}_{1.3}$ as solid electrolytes. After 100 cycles, the bare $\text{LiNi}_{0.8}\text{Mn}_{0.1}\text{Co}_{0.1}\text{O}_2$ cathode shows a discharge capacity of 61.8, 13.5, and 15.3 mAh/g, with a corresponding capacity retention of 44.0%, 11.7%, and 14.7%, respectively. Whereas, LiNbO_3 -coated cathode displays a discharge capacity of 83.4, 80.6, and 74.7 mAh/g, and a Coulombic efficiency of 59.23%, 66.6%, 78.3%. As shown in Fig. 5(d–f), LiNbO_3 -coated cathode shows much better cyclability and capacity properties at higher current density (0.382 and 0.764 mA/cm^2) than that at low current density (0.255 mA/cm^2). Moreover, as shown in Fig. S1(b), the discharge capacity of LiNbO_3 -coated cathode combined with $\text{Li}_6\text{PS}_5\text{Cl}$ electrolyte after 100 cycles is 61.4 mAh/g, which is much

smaller than the value of solid-state battery using LiNbO_3 -coated cathode and $\text{Li}_{5.7}\text{PS}_{4.7}\text{Cl}_{1.3}$ electrolytes. Previous research has shown that the bare $\text{LiNi}_{0.8}\text{Mn}_{0.1}\text{Co}_{0.1}\text{O}_2$ cathode suffers from a severe polarization effect during cycling, which can be mitigated after LiNbO_3 coating [45]. To clarify the effect of the LiNbO_3 coating, the galvanostatic intermittent titration technique (GITT) was employed to probe the polarization during the first three cycling processes. The transient charge/discharge voltage curves and the polarization for solid-state batteries using bare $\text{LiNi}_{0.8}\text{Mn}_{0.1}\text{Co}_{0.1}\text{O}_2$ cathode and LiNbO_3 -coated $\text{LiNi}_{0.8}\text{Mn}_{0.1}\text{Co}_{0.1}\text{O}_2$ cathode as active materials are shown in Fig. 5(g–i). The bare $\text{LiNi}_{0.8}\text{Mn}_{0.1}\text{Co}_{0.1}\text{O}_2$ cathode shows much higher polarization during the first three cycles compared to that of the LiNbO_3 -coated $\text{LiNi}_{0.8}\text{Mn}_{0.1}\text{Co}_{0.1}\text{O}_2$ cathode, as shown in Fig. 5(h and i). Our GITT results proved that the polarization of $\text{LiNi}_{0.8}\text{Mn}_{0.1}\text{Co}_{0.1}\text{O}_2$ cathode can be greatly reduced by coating with LiNbO_3 , yielding enhanced cycling performances. To investigate the interfacial resistance changes, EIS of solid-state batteries using the bare $\text{LiNi}_{0.8}\text{Mn}_{0.1}\text{Co}_{0.1}\text{O}_2$ cathode and the LiNbO_3 -coated $\text{LiNi}_{0.8}\text{Mn}_{0.1}\text{Co}_{0.1}\text{O}_2$ cathode were performed before and after 100 cycles under various current densities, the results of which are shown in Fig. 6. It appears that all of these impedance plots of fresh cells for both the bare $\text{LiNi}_{0.8}\text{Mn}_{0.1}\text{Co}_{0.1}\text{O}_2$ cathode and the LiNbO_3 -coated $\text{LiNi}_{0.8}\text{Mn}_{0.1}\text{Co}_{0.1}\text{O}_2$ cathode contains an arc at the high frequencies and a sharp line at the lower frequencies. The intersection of the arc with the Z' axis represents the resistance of the

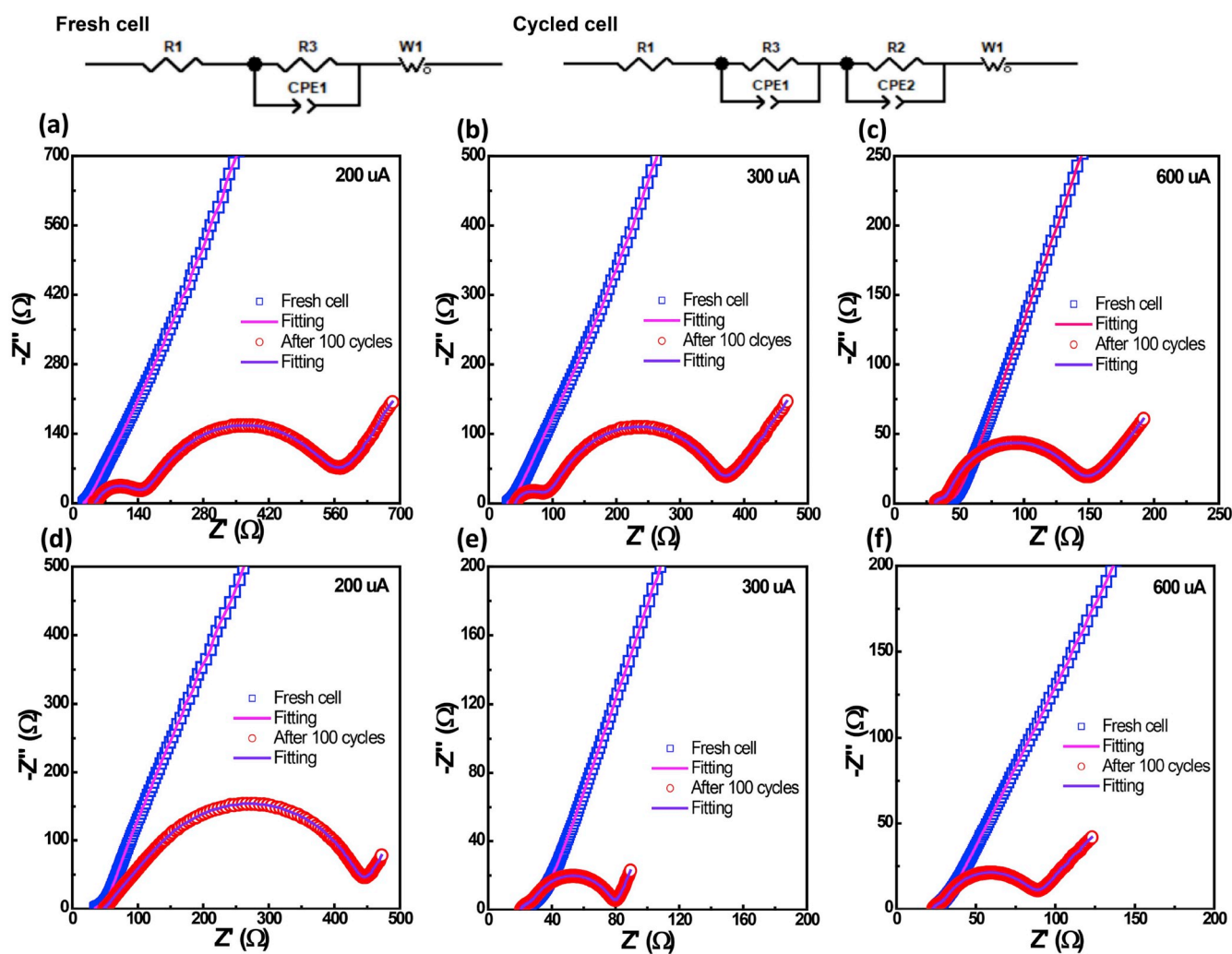


Fig. 6. The electrochemical impedance spectra of the solid-state lithium batteries using bare $\text{LiNi}_{0.8}\text{Mn}_{0.1}\text{Co}_{0.1}\text{O}_2$ (a, b, c) and LiNbO_3 -coated $\text{LiNi}_{0.8}\text{Mn}_{0.1}\text{Co}_{0.1}\text{O}_2$ (d, e, f) before and after 100 cycles under different charge/discharge current densities (200, 300, and 600 μA) at room temperature. The open squares and the open circles represent the fresh battery and the solid-state batteries after 100 cycles, respectively. The solid lines represent the fitting results.

solid electrolyte layer in the battery, while the arc part reflects the resistance between the active material and the lithium argyrodite solid electrolyte in the cathode mixture. After 100 cycles, all of these impedance plots consist of a tiny arc at the high frequencies, a semicircle at the middle frequencies, and a tail in the low frequencies. For the bare $\text{LiNi}_{0.8}\text{Mn}_{0.1}\text{Co}_{0.1}\text{O}_2$ electrode, the arc and the semicircle represent the resistance between the side reaction layer [2] and the active $\text{LiNi}_{0.8}\text{Mn}_{0.1}\text{Co}_{0.1}\text{O}_2$ and the resistance between the side reaction layer and the solid electrolyte, respectively. While for the LiNbO_3 -coated $\text{LiNi}_{0.8}\text{Mn}_{0.1}\text{Co}_{0.1}\text{O}_2$ electrode, the corresponding parts reflect the resistance between the LiNbO_3 coating layer and the $\text{LiNi}_{0.8}\text{Mn}_{0.1}\text{Co}_{0.1}\text{O}_2$ inner particle and the resistance between the LiNbO_3 coating layer and the lithium argyrodite solid electrolyte. As shown in Fig. 6a–f, the resistances of the solid electrolytes change slightly before and after 100 cycles for both the bare $\text{LiNi}_{0.8}\text{Mn}_{0.1}\text{Co}_{0.1}\text{O}_2$ and the LiNbO_3 -coated $\text{LiNi}_{0.8}\text{Mn}_{0.1}\text{Co}_{0.1}\text{O}_2$ solid-state batteries, while the resistances between the active $\text{LiNi}_{0.8}\text{Mn}_{0.1}\text{Co}_{0.1}\text{O}_2$ and lithium argyrodite solid electrolytes change obviously. The LiNbO_3 -coated $\text{LiNi}_{0.8}\text{Mn}_{0.1}\text{Co}_{0.1}\text{O}_2$ cathode displays much smaller interfacial resistance between the $\text{LiNi}_{0.8}\text{Mn}_{0.1}\text{Co}_{0.1}\text{O}_2$ particles and the lithium argyrodite solid electrolyte than that of the bare $\text{LiNi}_{0.8}\text{Mn}_{0.1}\text{Co}_{0.1}\text{O}_2$ cathode at both charge/discharge current densities [43–46]. It should be noticed that the interfacial resistance between the cathode and solid electrolyte for the solid-state batteries using bare $\text{LiNi}_{0.8}\text{Mn}_{0.1}\text{Co}_{0.1}\text{O}_2$ cathode decreases with increasing charge/discharge current densities. Previous researches have reported that side reaction happens between the bare layered structure cathode and sulfide electrolytes without the coating layer [45,47]. When the solid-state battery was cycled with a lower current density, the cycling time lasts much longer than the battery cycled at a larger current density, yielding much worse side reactions. Similar results were also found after the LiNbO_3 coating in Fig. 6(d–f). This conclusion is also confirmed in our ongoing work using lithium sulfide solid electrolyte as the active material for solid-state batteries. Therefore, the improved cycling performance of the LiNbO_3 -coated $\text{LiNi}_{0.8}\text{Mn}_{0.1}\text{Co}_{0.1}\text{O}_2$ cathode is due to the mitigation of polarization and the reduction in the interfacial resistance between the cathode and solid electrolyte.

4. Conclusions

Lithium ion conductivity of $\text{Li}_6\text{PS}_5\text{Cl}$ was improved by introducing Cl in the structure to increase the lithium vacancy. Among the modified lithium argyrodite structures $\text{Li}_{7-x}\text{PS}_{6-x}\text{Cl}_x$ ($x = 1.1, 1.2, 1.3, 1.4, 1.5, 1.6, 1.7, 1.8, \text{ and } 1.9$), $\text{Li}_{5.7}\text{PS}_{4.7}\text{Cl}_{1.3}$ was found to possess the highest lithium ion conductivity, up to 6.4 mS/cm at room temperature, and can be synthesized at 350 °C for 15 h. Lower annealing temperature is suitable for small doping amount of Cl to get pure phases with high lithium ion conductivity, while increasing the annealing temperature can promote the ionic conductivity of large doping amount of Cl, $\text{Li}_{7-x}\text{PS}_{6-x}\text{Cl}_x$ ($x = 1.7, 1.8, \text{ and } 1.9$). The lithium mobility of lithium argyrodite can be enhanced by Cl doping as demonstrated both by temperature-dependent AC impedance and ^7Li spin-lattice relaxation measurements. *Ab initio* molecular dynamics (AIMD) simulations results showed that the energy barriers for lithium ion migration in both short and long diffusion length scales decrease due to the introduction of Cl in the Li_6S group. Combined with an ALD-coated LiNbO_3 on $\text{LiNi}_{0.8}\text{Mn}_{0.1}\text{Co}_{0.1}\text{O}_2$ as the cathode and indium foil as the anode, $\text{Li}_{5.7}\text{PS}_{4.7}\text{Cl}_{1.3}$ shows excellent electrochemical performance, delivering an initial discharge capacity of 140.8 mAh/g at 0.255 mA/cm² and retaining 130.1 mAh/g after 50 cycles. LiNbO_3 coating is an effective route to improve the cyclability of $\text{LiNi}_{0.8}\text{Mn}_{0.1}\text{Co}_{0.1}\text{O}_2$ using lithium argyrodite solid electrolyte at various charge/discharge current densities due to the mitigation polarization and the reduced interfacial resistance between the cathode and solid electrolyte.

Declaration of competing interest

There are no conflicts to declare.

Acknowledgment

This work was supported by Natural Sciences and Engineering Research Council of Canada (NSERC), Canada Research Chair Program (CRC), Ontario Research Fund (ORF), GLABAT Solid-State Battery Inc., China Automotive Battery Research Institute, Canada Foundation of Innovation (CFI), and The University of Western Ontario.

Appendix A. Supplementary data

Supplementary data to this article can be found online at <https://doi.org/10.1016/j.nanoen.2019.104396>.

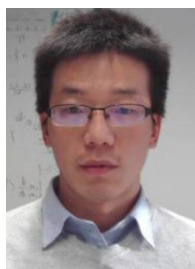
References

- [1] C. Yu, S. Ganapathy, N.J.J. de Klerk, I. Roslon, E.R.H. van Eck, A.P.M. Kentgens, M. Wagemaker, *J. Am. Chem. Soc.* 138 (2016) 11192–11201.
- [2] C. Yu, S. Ganapathy, E.R. Van Eck, H. Wang, S. Basak, Z. Li, M. Wagemaker, *Nat. Commun.* 8 (2017) 1086.
- [3] C. Wang, K.R. Adair, J. Liang, X. Li, Y. Sun, X. Li, J. Wang, Q. Sun, F. Zhao, X. Lin, *Adv. Funct. Mater.* (2019) 1900392.
- [4] C. Wang, X. Li, Y. Zhao, M.N. Banis, J. Liang, X. Li, Y. Sun, K.R. Adair, Q. Sun, Y. Liu, *Small Methods* (2019) 1900261.
- [5] Y. Kato, S. Hori, T. Saito, K. Suzuki, M. Hirayama, A. Mitsui, M. Yonemura, H. Iba, R. Kanno, *Nat. Energy* 1 (2016) 16030.
- [6] C. Cao, Z.-B. Li, X.-L. Wang, X.-B. Zhao, W.-Q. Han, *Front. Energy Res.* 2 (2014) 25.
- [7] Z. Gao, H. Sun, L. Fu, F. Ye, Y. Zhang, W. Luo, Y. Huang, *Adv. Mater.* 30 (2018) 1705702.
- [8] Y.S. Jung, D.Y. Oh, Y.J. Nam, K.H. Park, *Isr. J. Chem.* 55 (2015) 472–485.
- [9] J.C. Bachman, S. Muiy, A. Grimaud, H.-H. Chang, N. Pour, S.F. Lux, O. Paschos, F. Maglia, S. Lupart, P. Lamp, *Chem. Rev.* 116 (2015) 140–162.
- [10] L. Chen, Y. Li, S.-P. Li, L.-Z. Fan, C.-W. Nan, J.B. Goodenough, *Nano Energy* 46 (2018) 176–184.
- [11] R. Murugan, V. Thangadurai, W. Weppner, *Angew. Chem. Int. Ed.* 46 (2007) 7778–7781.
- [12] B. Boukamp, R. Huggins, *Mater. Res. Bull.* 13 (1978) 23–32.
- [13] B. Boukamp, R. Huggins, *Phys. Lett. A* 58 (1976) 231–233.
- [14] Y. Inaguma, L. Chen, M. Itoh, T. Nakamura, *Solid State Ion.* 70 (1994) 196–202.
- [15] H.J. Deiseroth, S.T. Kong, H. Eckert, J. Vannahme, C. Reiner, T. Zaiß, M. Schlosser, *Angew. Chem. Int. Ed.* 47 (2008) 755–758.
- [16] T. Asano, A. Sakai, S. Ouchi, M. Sakaida, A. Miyazaki, S. Hasegawa, *Adv. Mater.* 30 (2018) 1803075.
- [17] S. Wang, Q. Bai, A.M. Nolan, Y. Liu, S. Gong, Q. Sun, Y. Mo, *Angew. Chem. Int. Ed.* 58 (2019) 8039–8043.
- [18] C. Yu, S. Ganapathy, E.R. van Eck, L. van Eijck, N. de Klerk, E.M. Kelder, M. Wagemaker, *J. Energy Chem.* 38 (2019) 1–7.
- [19] C. Yu, S. Ganapathy, J. Hageman, L. van Eijck, E.R. van Eck, L. Zhang, T. Schwieter, S. Basak, E.M. Kelder, M. Wagemaker, *ACS Appl. Mater. Interfaces* 10 (2018) 33296–33306.
- [20] C. Yu, S. Ganapathy, E.R.H. van Eck, L. van Eijck, S. Basak, Y. Liu, L. Zhang, H. Zandbergen, M. Wagemaker, *J. Mater. Chem.* 5 (2017) 21178–21188.
- [21] C. Yu, J. Hageman, S. Ganapathy, L. van Eijck, L. Zhang, K.R. Adair, X. Sun, M. Wagemaker, *J. Mater. Chem.* 7 (2019) 10412–10421.
- [22] C. Yu, L. van Eijck, S. Ganapathy, M. Wagemaker, *Electrochim. Acta* 215 (2016) 93–99.
- [23] S. Boulineau, M. Courty, J.-M. Tarascon, V. Viallet, *Solid State Ion.* 221 (2012) 1–5.
- [24] S. Yubuchi, M. Uematsu, C. Hotehama, A. Sakuda, A. Hayashi, M. Tatsumisago, *J. Mater. Chem.* 7 (2019) 558–566.
- [25] P. Rayavarapu, N. Sharma, V. Peterson, S. Adams, *J. Solid State Electrochem.* 16 (2012) 1807–1813.
- [26] N.J. De Klerk, I. Roslon, M. Wagemaker, *Chem. Mater.* 28 (2016) 7955–7963.
- [27] J. VandeVondele, M. Krack, F. Mohamed, M. Parrinello, T. Chassaing, J. Hutter, *Comput. Phys. Commun.* 167 (2005) 103–128.
- [28] J.P. Perdew, *Phys. Rev. B* 33 (1986) 8822.
- [29] P. Janthon, S.M. Kozlov, F. Vines, J. Limtrakul, F. Illas, *J. Chem. Theory Comput.* 9 (2013) 1631–1640.
- [30] P. Janthon, S. Luo, S.M. Kozlov, F. Vines, J. Limtrakul, D.G. Truhlar, F. Illas, *J. Chem. Theory Comput.* 10 (2014) 3832–3839.
- [31] B.G. Lippert, J.H. Parrinello, Michele, *Mol. Phys.* 92 (1997) 477–488.
- [32] J. VandeVondele, J. Hutter, *J. Chem. Phys.* 127 (2007) 114105.
- [33] S. Goedecker, M. Teter, J. Hutter, *Phys. Rev. B* 54 (1996) 1703.
- [34] S. Nosé, *J. Chem. Phys.* 81 (1984) 511–519.
- [35] B. Wang, Y. Zhao, M.N. Banis, Q. Sun, K.R. Adair, R. Li, T.-K. Sham, X. Sun, *ACS Appl. Mater. Interfaces* 10 (2018) 1654–1661.
- [36] R.P. Rao, N. Sharma, V. Peterson, S. Adams, *Solid State Ion.* 230 (2013) 72–76.
- [37] S. Ganapathy, C. Yu, E.R. van Eck, M. Wagemaker, *ACS Energy Lett.* 4 (2019) 1092–1097.
- [38] V. Epp, O.z.l. Gün, H.-J.r. Deiseroth, M. Wilkening, *J. Phys. Chem. Lett.* 4 (2013) 2118–2123.
- [39] I. Hanghofer, M. Brinek, S. Eisbacher, B. Bitschnau, M. Volck, V. Hennige, I. Hanzu, D. Rettenwander, H. Wilkening, *Phys. Chem. Chem. Phys.* 21 (2019) 8489–8507.

- [40] H. Buschmann, J. Dölle, S. Berendts, A. Kuhn, P. Bottke, M. Wilkening, P. Heitjans, A. Senyshyn, H. Ehrenberg, A. Lotnyk, *Phys. Chem. Chem. Phys.* 13 (2011) 19378–19392.
- [41] P. Adeli, J.D. Bazak, K.H. Park, I. Kochetkov, A. Huq, G.R. Goward, L.F. Nazar, *Angew. Chem. Int. Ed.* 58 (2019) 8681–8686.
- [42] G. Oh, M. Hirayama, O. Kwon, K. Suzuki, R. Kanno, *Chem. Mater.* 28 (2016) 2634–2640.
- [43] W. Zhang, T. Leichtweiß, S.P. Culver, R. Koerver, D. Das, D.A. Weber, W.G. Zeier, J. r. Janek, *ACS Appl. Mater. Interfaces* 9 (2017) 35888–35896.
- [44] N. Ohta, K. Takada, I. Sakaguchi, L. Zhang, R. Ma, K. Fukuda, M. Osada, T. Sasaki, *Electrochem. Commun.* 9 (2007) 1486–1490.
- [45] X. Li, L. Jin, D. Song, H. Zhang, X. Shi, Z. Wang, L. Zhang, L. Zhu, *J. Energy Chem.* 40 (2020) 39–45.
- [46] W. Zhang, D.A. Weber, H. Weigand, T. Arlt, I. Manke, D. Schröder, R. Koerver, T. Leichtweiss, P. Hartmann, W.G. Zeier, *ACS Appl. Mater. Interfaces* 9 (2017) 17835–17845.
- [47] S.P. Culver, R. Koerver, W.G. Zeier, J. Janek, *Adv. Energy Mater.* (2019) 1900626.



Dr. Chuang Yu is currently a Postdoc in Prof. Xueliang (Andy) Sun's Group at the University of Western Ontario, Canada. He received his Ph.D. degree in Material Chemistry from TU Delft (Delft, the Netherlands) in 2017. His current research interests focus on the synthesis and conduction mechanism of sulfide solid electrolytes and its applications in all-solid-state batteries.



Yong Li is currently a research assistant under the supervision of Prof. Dr. Marcus Bäumer in the University of Bremen. His research interests mainly focus on revealing the correlation between physicochemical phenomena and electronic structure. Topics of computational electronic structure and electrocatalysis, photocatalysis, enzymatic catalysis, thermocatalysis, and batteries are involved



Dr. Mathew Willans received his Ph.D. in Chemistry under the supervision of Prof. Roderick Wasylshen at the University of Alberta, Canada in 2008. The same year, he began his current position as the manager of the JB Stothers NMR Facility at the University of Western Ontario, Canada. He specializes in utilizing solid-state NMR to study the structure and dynamics of a wide variety of small molecules and polymers.



Dr. Yang Zhao is currently a Postdoc in Prof. Xueliang (Andy) Sun's Group at the University of Western Ontario, Canada. He received his Ph.D. degree in Andy's Group at the University of Western Ontario (Canada) in 2019. His current research interests focus on atomic/molecular layer deposition in the application of lithium/sodium ion batteries and all solid-state batteries.



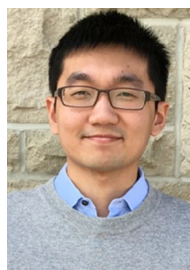
Keegan Adair received his B.Sc. in chemistry from the University of British Columbia in 2016. He is currently a Ph.D. candidate in Prof. Xueliang (Andy) Sun's Nanomaterials and Energy Group at the University of Western Ontario, Canada. Keegan has previously worked on battery technology at companies such as E-One Moli Energy and General Motors. His research interests include the design of nanomaterials for lithium metal batteries and nanoscale interfacial coatings for battery applications.



Feipeng Zhao is currently a Ph.D. candidate in Prof. Xueliang (Andy) Sun's Group at the University of Western Ontario, Canada. He received his B.S. degree and M.S. degree in Materials Science from Soochow University in 2017 and 2014, respectively. Currently, he is working on the synthesis and characterization of sulfide electrolytes, and development of high-performance solid-state Li metal and Na metal batteries.



Weihan Li completed his doctorate in material sciences under the supervision of Prof. Yan Yu at the University of Science and Technology of China, Hefei in 2016. He is currently a postdoctoral fellow at Prof. Xueliang (Andy) Sun's Nanomaterials and Energy Group at the University of Western Ontario, Canada. His research interests mainly include synthesis and application of nanomaterials for lithium-ion battery and sodium-ion battery.



Dr. Sixu Deng is currently a Ph.D. candidate in Prof. Xueliang (Andy) Sun's Group at the University of Western Ontario, Canada. He received his B.Eng. and Ph.D. degree of Materials Science and Engineering from Beijing University of Technology in 2011 and 2018, respectively. His research interests focus on cathode materials for lithium-ion batteries, sulfide and halide solid-state electrolytes, and all-solid-state lithium-ion batteries.



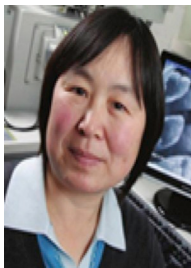
Dr. Jianwen Liang received his Ph.D. degree in inorganic chemistry from University of Science and Technology of China in 2015. He is currently a postdoctoral fellow in Prof. Xueliang (Andy) Sun's Nanomaterials and Energy Group at the University of Western Ontario, Canada. His research interests include sulfide-based solid-state electrolyte as well as all-solid-state Li/Li-ion batteries.



Dr. Mohammad Norouzi Banis is a research engineer in Prof. Xueliang (Andy) Sun's group at the University of Western Ontario, Canada. He received his Ph.D. degree in 2013 in Materials Science and Engineering from Western University, on the study of nanostructured low temperature fuel cells and application of x-ray absorption spectroscopy in energy related systems. His current research interests include study of metal ion, metal air and nanocatalysts via in-situ synchrotron-based techniques.



Dr. Rong Yang received his Ph.D. degree in inorganic chemistry from Peking University in 2011. He is currently a senior engineer in China Automotive Battery Research Institute. His research interests are focused on cathode materials for lithium-ion batteries, solid-state lithium ion conductors, and solid-state lithium-ion batteries.



Ruying Li is a research engineer at Prof. Xueliang (Andy) Sun's Nanomaterial and Energy Group at the University of Western Ontario, Canada. She received her master in Material Chemistry under the direction of Prof. George Thompson in 1999 at University of Manchester, UK, followed by work as a research assistant under the direction of Prof. Keith Mitchell at the University of British Columbia and under the direction of Prof. Jean-Pol Dodelet at l'Institut national de la recherche Scientifique (INRS), Canada. Her current research interests are associated with synthesis and characterization of nanomaterials for electrochemical energy storage and conversion.



Dr. Shigang Lu is Vice president of China Automotive Battery Research Institute Co., Ltd. He has the responsibility for technology innovations in the area of automotive battery application. He has extensive experience in many energy research areas including fuel cells, and lithium-ion batteries. Dr. Lu received her Ph.D. degree in Chemistry from Moscow State University in 1993. He has extensive experience in novel material processing techniques for automotive battery applications. His current research interests include new energy electrochemistry, lithium-ion battery and related materials, solid-state battery and related materials.



Dr. Huan (Henry) Huang received his Ph.D. from University of Waterloo in 2002. He is currently a General Manager for the company. He has extensive experience in lithium ion cylindrical cells and serves as a Research Scientist at E-One Moli Energy Corp., before managing GLABAT. His research interests focus on the development and commercialization of solid-state batteries with robust and consistent performance.



Dr. Yining Huang was born in Beijing, China. He obtained his B.Sc and M.Sc from Peking University and earned his Ph.D. from McGill University (Montreal, Canada). After an NSERC post-doctoral fellowship at the University of British Columbia (Vancouver, Canada), he started his independent academic career at Laurentian University (Sudbury, Ontario, Canada) as an Assistant Professor. He is currently Full Professor and the Chair in the Department of Chemistry, The University of Western Ontario (London, Ontario, Canada). Dr. Huang has published more than 220 peer-reviewed papers. His current research interest focuses on characterization of inorganic materials by solid-state NMR and vibrational spectroscopy.



Dr. Li Zhang is currently a senior scientist of China Automotive Battery Research Institute Co., Ltd., Beijing, China. He received his Ph.D. degree in Electrochemistry from University of Science & Technology Beijing, China in 2009. He has more than 10 years of power sources experience with expertise in battery materials as well as electrode design. Currently, his research interests include solid-state electrolytes, all-solid-state Li-air, and lithium batteries.



Prof. Xueliang (Andy) Sun is a Canada Research Chair in Development of Nanomaterials for Clean Energy, Fellow of the Royal Society of Canada and Canadian Academy of Engineering and Full Professor at the University of Western Ontario, Canada. Dr. Sun received his Ph.D. in materials chemistry in 1999 from the University of Manchester, UK, which he followed up by working as a postdoctoral fellow at the University of British Columbia, Canada and as a Research Associate at L'Institut National de la Recherche Scientifique (INRS), Canada. His current research interests are focused on advanced materials for electrochemical energy storage and conversion, including electrocatalysis in fuel cells and electrodes in lithium-ion batteries and metal-air batteries.